Atmos. Chem. Phys. Discuss., https://doi.org/10.5194/acp-2018-477
Manuscript under review for journal Atmos. Chem. Phys.
Discussion started: 25 June 2018

Atmospheric Chemistry and Physics
Open Access
Discussions

Secondary organic aerosol formation from photooxidation of furan: effects of NOx level and humidity

Xiaotong Jiang[1], Narcisse T. Tsona[1], Long Jia[2], Shijie Liu[1], Yongfu Xu[2], Lin Du[1]

[1] Environment Research Institute, Shandong University, Qingdao, 266237, China
[2] State Key Laboratory of Atmospheric Boundary Layer Physics and Atmospheric Chemistry, Institute of Atmospheric Physics, Chinese Academy of Sciences, Beijing, 100029, China

Correspondence to: Lin Du (lindu@sdu.edu.cn)

Abstract. Atmospheric furan is both primary and secondary pollutants in the atmosphere, and their emission contributes to the formation of ultrafine particles and ground-level ozone. We investigate the effects of NOx level and humidity on the formation of secondary organic aerosol (SOA) generated from the photooxidation of furan in the presence of NaCl seed particles. The particle mass concentration and size distribution were determined with a scanning mobility particle sizer (SMPS). SOA mass concentration and yield were determined under different NOx and humidity levels. Owing to condensation and coagulation, the particle number concentration decreases with increasing particle size. A significant difference is observed both in the SOA mass concentration and SOA yield variation with the initial experiment conditions. A relatively high NOx level, ranging from 16.8 to 97.5 ppb, contributes to effective formation of SOA in the presence of NaCl seed particles, with the mass concentration of SOA and SOA yield ranging from 0.96 μg m^{-3} to 23.46 μg m^{-3} and from 0.04 % to 1.01 %, respectively. Likewise, the SOA mass concentration and yield increase with increasing humidity, because the increasing RH increases the aerosol liquid water content, which contributes to the liquid phase reactions. Nine organic nitrate species were detected by electrospray ionization exactive orbitrap mass spectrometry (ESI-Exactive-Orbitrap MS). The -COOH，-OH，-C=O and NO_2 functional groups were assigned in the FTIR spectra and used as the indicator for the mechanism inference. The present study directly addresses NOx effects and reinforces the implication of humidity on SOA formation during the furan-NOx-NaCl photooxidation. Furthermore, the results illustrate the importance of studying SOA formation over a comprehensive range of environmental conditions. Only such evaluations can induce meaningful SOA mechanisms to be implemented in air quality models.

1 Introduction

Atmospheric particulate matter (PM) does not only have public effects such as human health and life expectancy, but also has adverse influence on visibility and global climate forcing (Hallquist et al., 2009; Pope et al., 2013). PM is primarily composed of organic carbon, black carbon, brown carbon, sulfate, nitrate, and other inorganic components (Donahue et al., 2009; Zhang et al., 2011b). Secondary organic aerosols (SOA) constitute a substantial portion of the total ambient aerosol particles, which mainly originate from biomass burning and atmospheric reactions of volatile organic compounds (VOCs)

(Kanakidou et al., 2005). Identifying the chemical composition and major precursors of SOA is helpful to better understand their formation mechanism and mastermind strategies for the control of PM. Aromatic hydrocarbons, which form a large fraction of nonmethane hydrocarbons, are regarded as important anthropogenic SOA precursors (Zhang et al., 2012b; Odum et al., 1997). Furthermore, aromatic compounds are important precursors of atmospheric O_3, with an estimated average contribution of O_3 formation potential of 75.5 % (Yin et al., 2015). Originated both from biomass burning and plant emission (Christian et al., 2003; Christian et al., 2004), furan is among the most abundant aromatic hydrocarbons in the atmosphere. Additionally, furan has been proved to be an essential intermediate in alkanes oxidation reactions (Russell et al., 2011). The SOA formation potential of furan has been studied in recent years (Cabanas et al., 2004; Liljegren and Stevens, 2013; Tapia et al., 2011), but its profound assessment in this formation is still poorly known. It is, however, likely that several factors including NOx levels and relative humidity (RH) would influence the implication of furan in SOA formation.

It is generally accepted that NOx level plays a critical role in SOA formation, by governing the reactions of organo-peroxy radicals (RO_2) (Song et al., 2005; Song et al., 2007). The branching ratio of RO_2 reactions with NOx and the hydroxperoxy radical (HO_2) are determined by the NOx level during the experiments (Kroll and Seinfeld, 2008). A previous study has asserted that the mechanisms of the two reactions differ sharply under different NOx level conditions. The RO_2 reacts only with NO under high NOx levels and with HO_2 under low NOx conditions (Ng et al., 2007). The latter case produces lower volatility products than the former one. The effect of NOx level on SOA formation has been investigated previously but results are inconclusive. A study focusing on the photooxidation of toluene and m-xylene has demonstrated that aerosol yields decrease as NOx level increases (Xu et al., 2015), while another study showed that the SOA yield from photooxidation of isoprene under high-NOx levels is 3 times more important than that measured under low NO_2/NO level (Chan et al., 2010). A different study indicated that under wet conditions, high initial NOx levels contribute effectively to SOA formation (Zhang et al., 2012a). This is in agreement with the observation for SOA formation from the irradiation of propylene that showed that SOA mass yield decreased with increasing propylene/NOx ratio (Ge et al., 2017b).

Besides the mixed effect of NOx level on SOA formation, the RH can significantly alter the sizes of SOA particles, depending on their hygroscopicity (Varutbangkul et al., 2006), their gas phase reactions involving water (Jonsson et al., 2006), and the aqueous chemistry occurring at their surfaces (Lim et al., 2010; Grgic et al., 2010). The photooxidation experiments of many aromatic compounds, such as toluene (Edney et al., 2000; Kamens et al., 2011; Cao and Jang, 2010; Faust et al., 2017; Hinks et al., 2018), benzene and ethylbenzene (Jia and Xu, 2014), m-xylene (Zhou et al., 2011), and 1,3,5-trimethylbezene (Cocker et al., 2001) have been carried out previously to study the RH effect on SOA formation. The results exhibited large discrepancies under different experimental conditions. The yield of SOA generated under low-NOx conditions was found to be small at high RH (Cao and Jang, 2010). A little RH effect was also observed on SOA particle formation and size distributions (Bonn and Moortgat, 2002; Fry et al., 2009). Nevertheless, positive correlations between RH and SOA yield have also been observed in the presence of hygroscopic seed particles (Kamens et al., 2011; Zhou et al., 2011), and the role of RH in SOA formation also appears to be mixed. Water vapor does not only participate in the VOC photooxidation reactions and affect the gas phase oxidation mechanisms, but also alters the partitioning of the reaction products between the gas phase and the particle phase, hereby influencing the equilibrium partitioning of generated organic aerosols (Spittler et al., 2006). Moreover, the RH is connected with SOA formation due to its strong influence on seed acidity and particle liquid water concentration (Mahowald et al., 2011). A high RH environment contributes to the increase of aerosol liquid water (ALW), which promotes the hydrolysis of organic compounds and lead to other heterogeneous reactions catalyzed by water (Ervens et al., 2011). Previous studies regarding the atmospheric reactions of furan typically focused on the kinetics and mechanism (Aschmann et al., 2014; Gomez Alvarez et al., 2009). To our knowledge, the study of RH effects and different NOx levels on SOA formation from photooxidation of furan has not been a subject of prior investigations.

In the present study, we used FTIR, in concert with SMPS to elucidate the roles of NOx level and RH in SOA formation from furan-NOx irradiation. All the experiments were conducted in the presence of NaCl seed particles, which are the second most abundant particles in atmosphere (Penkett, 1988). Specifically, we evaluate whether the increased ALW affects the SOA mass concentration and the SOA yield. The chemical composition of furan SOA was investigated by ESI-Exactive-Orbitrap MS, with focus on the formation of organic nitrates. Strong evidences that both the RH and different NOx levels have a significant effect on SOA formation from furan photooxidation are presented.

2 Experiments

2.1 SOA sample preparation

All experiments were performed in a 1.3 m^3 Teflon FEP film chamber at the Institute of Atmospheric Physics, Chinese Academy of Sciences, Beijing. To maximize and homogenize the interior light intensity, a mirror surface stainless steel was chosen as the interior wall of the enclosure. A total of 42 black-lamps (F40BLB, GE, Fairfield, CT, USA) with emission band centered at 365 nm were equipped in the facilities to simulate the spectrum of the UV band in solar irradiation. The chamber was equipped with multiple sampling ports, which allowed the introduction of clean air, seed aerosols, gas phase reagents, and for measurements of both gas phase and particle-phase compositions. The reaction setup used in the present study and the schematic of the smog chamber facility are shown in Fig. S1 (Liu et al., 2017; Jia and Xu, 2014, 2016; Ge et al., 2017a; Ge et al., 2017b).

The zero air (generated from Zero Air Supply, Model 111 and Model 1150, Thermo Scientific) was used as the background gas for the experiments, and three big hydrocarbon traps (BHT-4, Agilent, Santa Clara, CA, USA) coupled with three activated-carbon filters were used to get further purified air. The chamber was cleaned by flowing pure air for at least 4 h prior to each experiment, which ensured that all the NO, NO_2, NOx, and ozone concentrations were less than 1 ppb, and the particle concentration was lower than 10^{-3} cm^{-3}. The prepared gas phase furan was introduced into the chamber directly by a syringe. NOx was injected into the chamber by a gas-tight syringe. For the enhancement of the SOA formation, NaCl seed aerosols were injected into the chamber via atomization of NaCl aqueous solution with a constant-rate atomizer (Model 3076, TSI, USA). The liquid-droplet NaCl seed aerosol passed through a self-made diffusion dryer to reduce the liquid water content and reached the solid phase. An aerosol neutralizer (Model 3087, TSI, USA) was used to remove the electrostatic of particles before it was introduced into the reactor. The initial seed number and mass concentrations were approximately 5×10^4 cm^{-3} and 6 μg m^{-3} on average, respectively. The existential state of NaCl seed was determined by the degree of the RH. NaCl was solid when RH was below 45 % (Gao et al., 2007), and liquid droplets when RH was higher than 60 % (Ge et al., 2017a). For different RH conditions, the dry zero air was introduced into a bottle of high-purity water to control the humidity of the background air. The humidity in the chamber was detected with a hygrometer (Model 645, Testo AG, Lenzkirch, Germany). The initial experimental conditions considered in this study are summarized in Table 1. Typically, approximate 750 ppb furan and 5×10^4 cm^{-3} NaCl seed aerosols were employed. To study the effect of NOx levels on SOA formation, experiments were conducted under dry conditions, with initial furan/NOx ratios ranging from 7.83 to 48.15, whereas to develop and test the role of RH, experiments were performed for RH values varying from 5 to 85 % and with an initial average furan to NOx ratio of 7.55. The temperature of the chamber was controlled to be 308-310 K during all the experiments.

Particles and gas phase species may get lost to the chamber walls on short timescales, hereby influencing the gas phase chemistry and SOA formation. Previous studies determined wall loss rate constants of 4.1×10^{-7} s^{-1}, 3.3×10^{-7} s^{-1} and 3.6×10^{-5} s^{-1} for gaseous NO_2, O_3 and aerosol particles, respectively (Ge et al., 2016; Ge et al., 2017a). These values are considered in the present study. However, no wall loss of furan was observed within the uncertainty of the detection of the instrument. Furthermore, the light intensity in the reactor was determined to be 0.34 min^{-1} by using the NO_2 photolysis rate constant as the indirect representation. Before the start of every experiment, the static electricity of the Teflon chamber was removed. After all the reactants flowed into the chamber, the reactor was maintained in the dark for at least 40 min without any activities to reach homogeneous mixing.

2.2 Gas and particle monitoring

The concentrations of O_3 and NOx were measured continuously by UV photometric O_3 analyzer (Model 49C, Thermo Environmental Instruments Inc.) and a chemiluminescence analyzer (Model 42C, Thermo Electron Corporation, USA), respectively. The sampling flow rate was 1 L min^{-1} for both O_3 and NOx analyzers. The uncertainty in the gas phase measurements was below ± 1 %. The experiment samples were collected by Tenax absorption tubes (150 mm length × 6 mm O.D., 0.2 g sorbent). Furan concentrations and product samples were detected by thermal desorption-gas chromatography-mass spectrometry (TD-GC-MS): the thermal desorber (Master (Master TD, Dani, Italy) was combined with gas chromatography (Model 7890A, Agilent Tech., USA) interfaced to a mass selective detector (5975C, Agilent Tech., USA). The initial reactants concentrations are given in Table 1. The chromatographic analytical method used for the analysis was as follows: the chromatographic column was kept at 338 K for 4 min, then heated to 598 K at a heating rate of 20 K min^{-1} and held for 5 min.

The particle size distribution and mass concentration were measured with a scanning mobility particle sizer (SMPS, Model 3936, TSI, USA) composed of a TSI 3081 differential mobility analyzer (DMA) and a TSI 3776 condensation particle counter (CPC). The sampling and sheath flow rates of the SMPS were 0.3 L min^{-1} and 3 L min^{-1}, respectively. Given this flow conditions of the SMPS, particle sizes (in counts cm^{-3}) were recorded in 64 size bins for particles in the 13.6 to 710.5 nm size range. The accuracy of the particle number concentration is ±10 % at $<3\times10^5$ cm^{-3}. The method of the reduced Dry-Amibient Size spectrometer (DASS) was used to detect the ALW (Engelhart et al., 2011). To get dry particle mass concentrations, a large diameter Nafion dryer (Permapure MD-700-48F-3) and a multi-tube Nafion dryer (Permapure PD-200T-24E-M) were added to the sampling inlet and sheath flow, respectively. The results were compared with the mass concentrations detected in humid mode, in which the humid air in the chamber was introduced into the SMPS with the sheath air set at 10 L min^{-1}. The ALW was calculated as the difference between the particle mass concentrations determined at dry and humid modes (Jia and Xu, 2017). On the basis of the recorded particle volume concentration and assumed particle density, a total suspended particulate (TSP in μg m^{-3}) could be translated. As shown in Eq. (1), TSP is the sum of seed aerosol (NaCl in this work), $NaNO_3$, particle ALW, and SOA. By dissolving the SOA collected on ZnSe disks into high purity water, an ion chromatograph (IC, Dionex ICS-900, Thermo Fisher, USA) was then used to analyze the inorganic content (Cl^- and NO_3^-) in SOA. With known initial NaCl seed aerosol and their decay rates, the particle mass concentration of NaCl can be calculated, and based on the detected ALW during experiments, the SOA produced in the photooxidation of furan can be estimated from Eq. (1). However, there was no strong evidence of the existence of the ALW component when RH was below the deliquescence point of NaCl. The ALW was detected on the basis that the RH was above 54 %.

$$\mathrm{TSP} = \mathrm{NaCl} + \mathrm{NaNO_3} + \mathrm{ALW} + \mathrm{SOA} \qquad (1)$$

2.3 Chemical characterization of products

The SOA particles were sampled on ungreased ZnSe disk (25 mm in diameter) using a Dekati low-pressure impactor (DLPI, DekatiLtd, Kangasala, Finland) after the appearance of the O_3 maximum concentration. The sampling flow rate of DLPI was 10 L min^{-1} with the particles sizes from 30 nm to 10 μm, classified into 13 stages. According to the particle distribution explored from the SMPS, the SOA particles size was mainly around 150 nm after 3 h of irradiation. The ZnSe disk was placed on stage 3 to reach the maximum collection of the particles. Afterwards, the ZnSe disk was put in the FTIR (Nicolet iS10, Thermos Fisher, USA) sample holder, which had been flushing with N_2 to eliminate the impact of ambient H_2O and CO_2 on the determination of the chemical composition of formed SOA particles. The spectra were recorded at 4 cm^{-1} resolution with 128 scans. The samples collected on the ZnSe disk were then dissolved with high purity water for analyzing inorganic species.

To obtain chemical characterization information, the electrospray ionization exactive orbitrap mass spectrometry (ESI-Exactive-Orbitrap MS, Thermo Fisher, USA) was also used for the analysis of water-soluble organic aerosol (OA) produced from the photooxidation of furan. As a “soft ionization”, ESI can provide molecular formulae for thousands of OA substances when coupled with a high-resolution mass analyzer. The collected SOA samples were eluted with 1 mL of acetonitrile. The addition of acetonitrile allows a lower surface tension of the solution and provides a stable electrospray ionization process (Koch et al., 2005). Both positive (+) and negative (-) ion modes were chosen to operate. N_2 was used as the sheath and auxiliary gas.

3 Results and discussion

3.1 Gas phase and SMPS results

Experiments were divided into three groups, which were set to study the role of NOx and RH on SOA formation, and to analysis the ESI-Exactive-Orbitrap MS. To keep the variables of each set of conditions consistent, almost identical initial gas phase conditions were required. The addition of furan and seed aerosol in all the experiments was nearly equal. The first set of experiments (Exps.1- 6, Table 1), designed to investigate the effect of NOx level on SOA formation, used similar RH conditions with different NOx concentrations. For Exp.6- Exp.12, different RH levels coupled with similar furan/NOx ratios were monitored to assess the RH impact on SOA formation. Three experimental conditions were considered to analyze the ESI-Exactive-Orbitrap MS, which intended to compare the role of NOx and RH on the SOA formation. Fig. 1 shows the time dependence of gas phase concentrations of NO, NO_2, NOx, O_3 and the particle number/mass concentrations (wall loss corrected). The major gas phase inorganic chemical reactions occurred during the experiments are presented in Fig. S2. After turning on the light, the photolysis of NO_2 produced NO and O, which further reacted with O_2 to form O_3 in the chamber. The ozonolysis of furan contributes to the formation of OH radicals, which can also be formed through the photolysis of HONO, as well as the reaction of HO_2 and NO (Howard and Evenson, 1977). As a result, a slight increase in the beginning, followed by the decrease of NO concentrations are observed in Fig. 1. On the one hand, the decrease of NO is caused by the reaction between NO and alkyl peroxy radicals (RO_2), which are formed from the OH-initiated oxidation of furan during the experiment. On the other hand, the ozonation of NO also contributes to the NO decreasing trend. With the decrease of the NOx concentration, the concentration of O_3 increased rapidly in the beginning of the experiment to reach the maximum, and then remained constant throughout. Overall, the main sinks of furan are oxidations by O_3 and OH, and the reaction products are RO_2 and HO_2 radicals, which promote the cycling of O_3 formation by converting the NO back to NO_2.

As shown in Fig. 1, the profile of particle concentrations characteristics over time during the oxidation of furan (C_4H_4O/NOx=7.91, RH=23 %) exhibits a decrease in number concentration. We assume that the decay rate of the particle number concentration resulted from the coagulation of aerosol particles. With SOA formation, organics start to dominate and result in enhanced growth of clusters, which promote the decay of the particle number concentration (Kulmala et al., 2013). Correspondingly, the SOA mass concentration calculated based on the number concentration shows a fast increase with increasing O_3 concentration, with a slight decrease after reaching the maximum. This phenomenon may be caused by different chemical processes occurring during the experiments. In the beginning of the experiment, the gas phase reaction of RO_2 and NO was the dominant reaction path. However, as the reaction proceeds and the NO concentration gets lower, furan could still react with OH and produce the RO_2 radicals. The newly formed RO_2 could further react either with itself or with

HO_2 to form organic peroxides. A similar observation was reported by Zhang et al., who studied the SOA formation from the photooxidation of isoprene (Zhang et al., 2011a). Indeed, significant changes are observed in the particle number and mass concentrations before and after the reaction (Fig. S3), which further confirms the formation of SOA during the photooxidation of furan.

The calculated SOA yield is defined as the ratio of the mass concentrations of the maximum SOA formed (M_{SOA} in μg m^{-3}, corrected by wall loss) and the reacted furan (ΔC_4H_4O in μg m^{-3}):

$$Y_{SOA} = (\mathrm{M_{SOA}}/\Delta\mathrm{C_4H_4O})\times 100\ \% \qquad (2)$$

where M_{SOA} is obtained by subtracting the amount of NaCl and $NaNO_3$ from the total particle mass concentration measured by the SMPS, and ΔC_4H_4O is the consumption of furan during the experiments. Experiments were started with an average of 12.6 μg m^{-3} of NaCl seed aerosol and were conducted under different initial C_4H_4O/NOx ratios. After the photooxidation reactions, the SOA mass concentrations reached maxima between 0.96 μg m^{-3} and 23.46 μg m^{-3}, with SOA yield ranging from 0.04 % to 1.01 %. In other experiments carried out under varying RH conditions, SOA maxima were in the range of 23.46-119.29 μg m^{-3}, with SOA yield ranging from 1.01 % to 5.03 %.

3.2 Effects of NOx and RH on SOA formation

Fig. 2 shows the comparisons of the observed concentrations of O_3 and NOx from furan irradiations at different experimental conditions. It exhibits a sharper increase of O_3 formation at 42 % RH than that at 5 % RH. The O_3 maximum concentration was reduced by almost 60 % as the C_4H_4O/NOx ratio increased from 7.83 to 36.60. However, the effect of RH on O_3 formation is not so obvious compared to the difference in initial C_4H_4O/NOx ratio. The appearance time of O_3 maximum concentration at high C_4H_4O/NOx ratio is almost half an hour earlier than that at low initial C_4H_4O/NOx ratio. On the contrary, there is no significant difference on the balance time of NOx concentration under different experimental conditions. Similar initial C_4H_4O/NOx ratios result in similar profile of NOx concentration during the experiment, although the final NOx concentration shows slight difference.

To study the NOx level effect on SOA formation, the experiments were conducted with varying initial C_4H_4O/NOx ratios ranging from 7.83 to 48.15. The O_3 maximum concentration, SOA mass concentration and SOA yield dependences on the C_4H_4O/NOx ratio are presented in Fig. 3. The results show that the O_3 maximum concentration produced during the experiments decreases with increasing C_4H_4O/NOx ratio. When the C_4H_4O/NOx ratio decreases from 16.84 to 7.83, there is a sharp increase in O_3 concentration from 197 to 382 ppb. Interestingly, experiments for which the C_4H_4O/NOx ratio changed from 48.15 to 36.60 exhibit a change of 24 ppb in O_3 maximum concentration. This result indicates that under different C_4H_4O/NOx ratio regimes, the concentration of O_3 produced varies much. There is a great change in O_3 cumulation when the C_4H_4O/NOx ratios are relatively low (<16.84), which is consistent with a previous observation on C_3H_6-NOx-NaCl irradiation experiments by Ge et al. (Ge et al., 2017b) who found that when the C_3H_6/NOx ratio was less than 11, the O_3 concentration decreased considerably with increasing ratio, whereas when the ratio was larger than 11, the O_3 concentration slightly decreased with increasing ratio. In addition, the SOA is found to have much lower yield under a high C_4H_4O/NOx

Atmos. Chem. Phys. Discuss., https://doi.org/10.5194/acp-2018-477
Manuscript under review for journal Atmos. Chem. Phys.
Discussion started: 25 June 2018

ratio. The SOA mass concentration and SOA yield increased from 0.96 to 23.46 μg m^{-3} and 0.04 % to 1.01 %, respectively, as the initial concentration ratio of C_4H_4O/NOx decreased from 48.15 to 7.83 (ppbC/ppb). This trend is consistent with previous studies on propylene photooxidation, which found that the SOA yield was enhanced under a low VOC/NOx ratio (Ge et al., 2017b). Another laboratory observation of aerosol assessment from isoprene photooxidation concluded that under low NOx level (< 129 ppb), the SOA mass increased with increasing initial NOx level (Kroll et al., 2006). By comparing the studies of Ge et al. and Kroll et al., one may surmise there is a positive correlation between NOx effect and SOA formation when the initial NOx level is relatively low (nearly below 100 ppb). These results further support our findings in the experiments of furan photooxidation.

Experiments Exps.6-12 were conducted under seven different RH conditions. The dependences of O_3 maximum concentration, SOA mass concentration, SOA yield and ALW on RH are presented in Fig. 4. The O_3 maximum concentration was detected in each experiment. The O_3 maximum concentration decreased with increasing RH, whereas the SOA mass concentration and yield increased. This decrease in O_3 maximum concentration is likely due to the fact that high RH conditions favor the transformation of polar nitro (RNO_2) and nitrate ($RONO_2$) into the aerosol phase (reaction (R10)), which suppressed the reaction of RO and NO_2 (reaction (R7)), thus decreased the O_3 formation through the pathways of reactions (R1) and (R2) (Jia and Xu, 2016). Another possible explanation for this decrease might be the heterogeneous reaction of N_2O_5 with aerosol liquid water and NaCl particles as demonstrated by a previous work (Jia and Xu, 2014).

Under different RH conditions ranging from 5 % to 85 %, the SOA yield increases from 1.01 % to 5.03 %. Both the SOA mass and $NaNO_3$ concentrations increase with the increase of RH. With almost identical initial conditions except RH, furan-derived SOA formed at high RH can be a factor of two higher than that formed at low RH. A similar trend was also observed by Yu et al., who found that the SOA mass concentrations increased by a factor of six when RH increased from 18 % to 82 % (Yu et al., 2011). This phenomenon might result from the SOA formation through heterogeneous reaction and aqueous chemistry in wet aerosols (Grgic et al., 2010; Lim et al., 2010). In these atmospheric processes, alcohols, aldehydes and ketones formed from the photooxidation of furan in the gas phase can be absorbed into the humid surface of the hygroscopic SOA at high RH. This further contributes to the formation of low-volatility products on the SOA surface. It is noted that with the NaCl seed aerosols serving as nuclei, the ALW was generated at high RH. Products with water solubility produced from the photooxidation of furan can dissolve into the ALW on the surface of particle aerosols. As a result, ALW in the formed aerosols plays an important role in gas/particle partitioning. As shown in Fig. 4, the ALW was detected when the RH was higher than 54 %, which was based on the deliquescence of NaCl under high RH conditions. The increase of ALW could partially explain the increase of SOA mass concentration and SOA yield. It is highly probable that the particle surface area increases with the amount of ALW increasing, which likely promotes the dissolution of semi-volatile matters produced during the experiments. In addition, the aqueous photochemistry of highly soluble small compounds that portioned in ALW could produce additional organic compounds and result in larger SOA yield under high RH conditions (Faust et al., 2017; Jia and Xu, 2014). Another explanation for the prominent effect of RH on SOA mass concentration is related to the stronger hygroscopicity of SOA with the RH increasing. In fact, the hydrophilic functional groups (such as, -COOH, -OH, -CO and -

COH) at the SOA surface, which were produced during the photooxidation of furan, could absorb the water molecules (Jaoui et al., 2006). Therefore, it is possible that at high RH the produced SOA could partition into wet particle seeds and further contribute to air pollution. Contour plots of SOA bursts in Fig. S4 show that SOA are very quickly generated under high RH conditions with a wide particle diameter distribution. SOA formed under a low C_4H_4O/NOx ratio also have a faster increase than those under large C_4H_4O/NOx ratio conditions. However, the particle number distribution under conditions of C_4H_4O/NOx=7.83 and C_4H_4O/NOx=36.60 is equally relevant.

3.3 SOA chemical composition

To get detailed information on the functional groups in SOA formed during the photooxidation of furan, the collected particles were measured by FTIR, which has been proved to be an ideal technique for the detection of functional groups and bond information in aerosol samples. The FTIR spectra of particles collected from furan-NOx-NaCl with different values of C_4H_4O/NOx ratio are shown in Fig. 5. Obvious absorptions of organic functional groups were detected, which further confirmed the SOA formation from the photooxidation of furan. The assignment of the FTIR absorption frequencies is summarized in Table 2. The organic nitrate exhibits typical NO symmetric stretching at 868 cm^{-1}, NO_2 symmetric stretching at around 1341 cm^{-1}, and NO_2 asymmetric stretching at 1614 cm^{-1} (Jia and Xu, 2016). The absorption at 1067 cm^{-1} matches the C-O stretching vibration in C-O-C, while the sharp absorption at 1724 cm^{-1} is the C=O stretching vibration in carboxylic acid and ketones (Sakamoto et al., 2013). The carbon skeleton corresponds to the vibrations between 2850 cm^{-1} and 3100 cm^{-1}, where the ν(C-H) stretching vibration can be found. Absorptions in the ranges 2850-3000 cm^{-1} and 3000-3100 cm^{-1} represent the C-H stretching vibration in saturated carbon ring and unsaturated alkenes, respectively. Correspondingly, the H-C-H bending vibrations are represented by the absorption between 1350 and 1515 cm^{-1}. The strong broad vibrations at 2400-3500 cm^{-1} are interpreted as the O-H stretching vibration in carboxyl groups and hydroxyl groups (Ge et al., 2017b).

Fig. 5 illustrates the influence of NOx level on the SOA components during the photooxidation of furan. For each of the functional groups, experiments with the most pronounced SOA formation are those with the lowest initial C_4H_4O/NOx ratio. This is further confirmed by comparing the SOA yield for different NOx level conditions under approximately similar gas phase and initial seed conditions. The calculated variations of relative intensities of FTIR functional groups at different NOx levels are presented in Fig. 6. The carbonyl compound formed with 7.83 initial C_4H_4O/NOx ratio is approximately thrice more abundant than that formed with 48.15 initial C_4H_4O/NOx ratio. The absorbance of NO_2 functional groups exhibits a much stronger enhancement under initial C_4H_4O/NOx ratio of 7.83 compared to 48.15. Although at different C_4H_4O/NOx ratio conditions the intensities of C-O-C and O-H functional groups show similar trends, their variations are substantially different from the variations of other functional groups. In sum, the increased absorbance of functional groups with decreasing initial C_4H_4O/NOx ratios demonstrates that relatively high NOx level contributes to the formation of SOA.

The FTIR results of the investigation of furan photooxidation under different RH conditions are shown in Fig. 7. The absorbance of FTIR characteristic peak increases with the RH raising from 5 % to 85 %. Note that obvious intensities of the functional groups were observed when the RH exceeded the efflorescence RH of NaCl. In contrast, the absorptions of corresponding functional groups enhance gently when the RH is lower than 42 %. This phenomenon is consistent with the results of SOA yield discussed above and, can also be interpreted as the increasing ALW components contributing to SOA formation. The ratio of the absorbance intensities detected at low RH to that at 85 % RH is used as the relative intensity to show a more intuitive result of FTIR analysis. As shown in Fig. 8, for RH between 5 % to 37 %, the intensities of all functional groups vary weakly and are approximately one third of the intensity at 85 % RH. However, when the RH raises from 42 % to 85 %, the absorption intensities of O-H and NO_2 functional groups increase by factors of 2.0 and 1.9, respectively. In this RH range, the variations of relative intensities are even stronger for C=O, C-H and C-O-C, being increased by factors of 2.3, 2.3 and 2.5, respectively. A previous study has observed that in an urban environment containing aromatic hydrocarbons and NOx, the SOA yield increased by a factor of 2 to 3 under high RH compared to lower RH (Zhou et al., 2011). This trend is similar to that found in experiments with toluene in an urban aromatic hydrocarbon-NOx mixture system (Kamens et al., 2011). It should be pointed out that observed FTIR results show a high degree of consistency with the SOA mass concentration and SOA yield.

To further identify and confirm the structure of generated SOA components, more techniques, such as GC/MS and ESI-Exactive-Orbitrap MS were used to analyze the chemical composition. The first-generation products produced by the photooxidation of furan are not expected to partition directly into the particle phase according to their volatilities. As shown in Fig. S5, 1,2-dichloroethane, hydroxy-2-propanone, and butyl formate were detected by GC/MS in the gas phase. Three experiments of furan-NOx-NaCl photooxidation that were conducted under different initial C_4H_4O/NOx ratios and RH conditions were analyzed by ESI-Exactive-Orbitrap MS, and the MS spectra of generated species are shown in Fig. 9. The mass spectra recorded in different ion modes represent the detected compounds ionizable in either positive or negative modes (Walser et al., 2008). Although not reported here, we found that experiments preformed at relatively high initial C_4H_4O/NOx ratio (16.14) and high RH (79 %) conditions exhibit similar SOA components to those detected in the experiments performed under the conditions of 7.28 initial C_4H_4O/NOx ratio and 5 % RH. At 5 % RH, the chromatographic peaks obtained at C_4H_4O/NOx 7.28 ratio were found to be more intense than those obtained at 16.14 C_4H_4O/NOx ratio (Fig. S6). This is an indication that a relatively high NOx level contributes more to the SOA mass, however, without changing the composition of the SOA components. The peak intensities changes of SOA products detected in the positive mode were not obvious. However, increasing the RH resulted in an overall addition of peak intensities in the negative ion mode, due to the fact that the sample obtained at high RH during the SOA generation had a larger particle mass. For example, a relatively stronger intense band of $C_9H_{17}O_3N$ component (m/z=187) was found under a high RH. It is possible that the aqueous surface of seed particles provides a new substrate for the photooxidation of furan. Previously, N_2O_5 and HNO_3 have been proven to be the key products in the VOC-NOx irradiation experiments (Wang et al., 2016). Especially, N_2O_5 can easily react with the deliquescent NaCl seed particles under high RH conditions, forming $ClNO_2$ and $NaNO_3$ (Ravishankara, 2009). Furthermore, with the formation of acid components as shown in the FTIR results, acid-catalyzed reactions may occur during the experiment, which will promote the uptake of the semi-volatile products generated from the photooxidation of furan. Previous studies found that the uptake by acid-catalyzed reactions contributed to the formation of SOA (Riva et al., 2016;

Lin et al., 2012). Fig. 10 shows the sum of the ion mass peaks with *m/z* ranges in <200, 200-299, 300-399 and 400-499. The signals with *m/z* = 200-299 were more intense than the signals in other *m/z* ranges, for both positive and negative ion mode. Despite the changing of peak abundance, the major observed mass spectra peaks remained the same. Table 3 lists the five most abundant peaks detected in each ion mode for different experimental conditions. It follows that for each mode the dominating peaks are generally similar regardless the NOx level and RH conditions. This suggests that the major products are generated by a similar mechanism.

4 Atmospheric relevance and conclusion

The current study investigates the effects of NOx and RH on SOA formation from the photooxidation of furan in the presence of NaCl seed particles. The results show that a relatively high NOx level contributes efficiently to the formation of SOA, and the increase of RH results in the increase in the mass concentration of the generated SOA. The mechanisms controlling SOA formation may include the gas phase photooxidation of furan, physical water uptake as RH increases, the gas phase reaction of water with the first-generation products and the aqueous chemistry of low-volatility products reacting at the wet surface of NaCl seed particles. Seed aerosols are important for the growth of atmospheric particles and, therefore, affect aerosol-cloud-climate interactions. Organic nitrates, detected with FTIR and ESI-Exactive-Orbitrap MS, were found as significant components of new formed particles. The toxicity of ultrafine particles such as SOA is not only related to the atmospheric concentration but also to the nature and chemical properties of both the precursors and the formed SOA components. As a result, the detailed analysis and exact assignment of the chemical composition of SOA would help evaluate the health effects of SOA. The current results could also be used to interpret ambient gas phase measurements and reaction mechanisms inference. The inclusion of this reaction in current atmospheric models may improve the understanding of climate forcing of aerosols.

The influence of ALW component on SOA yield was examined and it was found that increased ALW amount leads to higher SOA mass concentration and yield, therefore highlighting the importance of the ALW in photooxidation reactions. A recent study showed that the reactive nitrogen chemistry in aerosol water can be a source of atmospheric sulfate during haze events (Cheng et al., 2016). In addition, the ALW is deeply linked with air quality (Malm et al., 1994) and aqueous SOA formation (Sareen et al., 2017). This is a further indication that the crucial role of ALW in atmospheric chemistry is vital to better understand the atmospheric physicochemical processes.

Acknowledgments

This work was supported by National Natural Science Foundation of China (91644214, 41375129) and Shandong Natural Science Foundation for Distinguished Young Scholars (JQ201705).

References

Aschmann, S. M., Nishino, N., Arey, J., and Atkinson, R.: Products of the OH radical initiated reactions of furan, 2-and 3-methylfuran, and 2,3-and 2,5-dimethylfuran in the presence of NO, J. Phys. Chem. A, 118, 457-466, 10.1021/jp410345k, 2014.

Bonn, B., and Moortgat, G. K.: New particle formation during alpha- and beta-pinene oxidation by O_3, OH and NO_3, and the influence of water vapour: Particle size distribution studies, Atmos. Chem. Phys., 2, 183-196, 10.5194/acp-2-183-2002, 2002.

Bruns, E. A., Perraud, V., Zelenyuk, A., Ezell, M. J., Johnson, S. N., Yu, Y., Imre, D., Finlayson-Pitts, B. J., and Alexander, M. L.: Comparison of FTIR and particle mass spectrometry for the measurement of particulate organic nitrates, Environ. Sci. Technol., 44, 1056-1061, 10.1021/es9029864, 2010.

Cabanas, B., Baeza, M. T., Salgado, S., Martin, P., Taccone, R., and Martinez, E.: Oxidation of heterocycles in the atmosphere: Kinetic study of their reactions with NO_3 radical, J. Phys. Chem. A, 108, 10818-10823, 10.1021/jp046524t, 2004.

Cao, G., and Jang, M.: An SOA model for toluene oxidation in the presence of inorganic aerosols, Environ. Sci. Technol., 44, 727-733, 10.1021/es901682r, 2010.

Chan, A. W. H., Chan, M. N., Surratt, J. D., Chhabra, P. S., Loza, C. L., Crounse, J. D., Yee, L. D., Flagan, R. C., Wennberg, P. O., and Seinfeld, J. H.: Role of aldehyde chemistry and NOx concentrations in secondary organic aerosol formation, Atmos. Chem. Phys., 10, 7169-7188, 10.5194/acp-10-7169-2010, 2010.

Cheng, Y., Zheng, G., Wei, C., Mu, Q., Zheng, B., Wang, Z., Gao, M., Zhang, Q., He, K., Carmichael, G., Poschl, U., and Su, H.: Reactive nitrogen chemistry in aerosol water as a source of sulfate during haze events in China, Sci. Rep., 2, 10.1126/sciadv.1601530, 2016.

Christian, T. J., Kleiss, B., Yokelson, R. J., Holzinger, R., Crutzen, P. J., Hao, W. M., Saharjo, B. H., and Ward, D. E.: Comprehensive laboratory measurements of biomass-burning emissions: 1. Emissions from Indonesian, African, and other fuels, J. Geophys. Res., 108, 1-13, 10.1029/2003jd003704, 2003.

Christian, T. J., Kleiss, B., Yokelson, R. J., Holzinger, R., Crutzen, P. J., Hao, W. M., Shirai, T., and Blake, D. R.: Comprehensive laboratory measurements of biomass-burning emissions: 2. First intercomparison of open-path FTIR, PTR-MS, and GC- MS/FID/ECD, J. Geophys. Res., 109, 1-12, 10.1029/2003jd003874, 2004.

Cocker, D. R., Mader, B. T., Kalberer, M., Flagan, R. C., and Seinfeld, J. H.: The effect of water on gas-particle partitioning of secondary organic aerosol: II. m-xylene and 1,3,5-trimethylbenzene photooxidation systems, Atmos. Environ., 35, 6073-6085, 10.1016/s1352-2310(01)00405-8, 2001.

Coury, C., and Dillner, A. M.: A method to quantify organic functional groups and inorganic compounds in ambient aerosols using attenuated total reflectance FTIR spectroscopy and multivariate chemometric techniques, Atmos. Environ., 42, 5923-5932, 10.1016/j.atmosenv.2008.03.026, 2008.

Donahue, N. M., Robinson, A. L., and Pandis, S. N.: Atmospheric organic particulate matter: From smoke to secondary organic aerosol, Atmos. Environ., 43, 94-106, 10.1016/j.atmosenv.2008.09.055, 2009.

Duarte, R., Pio, C. A., and Duarte, A. C.: Spectroscopic study of the water-soluble organic matter isolated from atmospheric aerosols collected under different atmospheric conditions, Anal. Chim. Acta, 530, 7-14, 10.1016/j.aca.2004.08.049, 2005.

Edney, E. O., Driscoll, D. J., Speer, R. E., Weathers, W. S., Kleindienst, T. E., Li, W., and Smith, D. F.: Impact of aerosol liquid water on secondary organic aerosol yields of irradiated toluene/propylene/NOx/$(NH_4)_2SO_4$/air mixtures, Atmos. Environ., 34, 3907-3919, 10.1016/s1352-2310(00)00174-6, 2000.

Engelhart, G. J., Hildebrandt, L., Kostenidou, E., Mihalopoulos, N., Donahue, N. M., and Pandis, S. N.: Water content of aged aerosol, Atmos. Chem. Phys., 11, 911-920, 10.5194/acp-11-911-2011, 2011.

Ervens, B., Turpin, B. J., and Weber, R. J.: Secondary organic aerosol formation in cloud droplets and aqueous particles (aqSOA): A review of laboratory, field and model studies, Atmos. Chem. Phys., 11, 11069-11102, 10.5194/acp-11-11069-2011, 2011.

Faust, J. A., Wong, J. P. S., Lee, A. K. Y., and Abbatt, J. P. D.: Role of aerosol liquid water in secondary organic aerosol formation from volatile organic compounds, Environ. Sci. Technol., 51, 1405-1413, 10.1021/acs.est.6b04700, 2017.

Fry, J. L., Kiendler-Scharr, A., Rollins, A. W., Wooldridge, P. J., Brown, S. S., Fuchs, H., Dube, W., Mensah, A., dal Maso, M., Tillmann, R., Dorn, H. P., Brauers, T., and Cohen, R. C.: Organic nitrate and secondary organic aerosol yield from NO_3

oxidation of beta-pinene evaluated using a gas-phase kinetics/aerosol partitioning model, Atmos. Chem. Phys., 9, 1431-1449, 10.5194/acp-9-1431-2009, 2009.

Gao, Y., Chen, S. B., and Yu, L. E.: Efflorescence relative humidity of airborne sodium chloride particles: A theoretical investigation, Atmos. Environ., 41, 2019-2023, 10.1016/j.atmosenv.2006.12.014, 2007.

Ge, S., Xu, Y., and Jia, L.: Secondary organic aerosol formation from ethyne in the presence of NaCl in a smog chamber, Environ. Chem., 13, 699-710, 10.1071/en15155, 2016.

Ge, S., Xu, Y., and Jia, J.: Secondary organic aerosol formation from ethylene ozonolysis in the presence of sodium chloride, J. Aerosol Sci., 106, 120-131, 10.1016/j.jaerosci.2017.01.009, 2017a.

Ge, S., Xu, Y., and Jia, L.: Secondary organic aerosol formation from propylene irradiations in a chamber study, Atmos. Environ., 157, 146-155, 10.1016/j.atmosenv.2017.03.019, 2017b.

Gomez Alvarez, E., Borras, E., Viidanoja, J., and Hjorth, J.: Unsaturated dicarbonyl products from the OH-initiated photo-oxidation of furan, 2-methylfuran and 3-methylfuran, Atmos. Environ., 43, 1603-1612, 10.1016/j.atmosenv.2008.12.019, 2009.

Grgic, I., Nieto-Gligorovski, L. I., Net, S., Temime-Roussel, B., Gligorovski, S., and Wortham, H.: Light induced multiphase chemistry of gas-phase ozone on aqueous pyruvic and oxalic acids, Phys. Chem. Chem. Phys., 12, 698-707, 10.1039/b914377g, 2010.

Hallquist, M., Wenger, J. C., Baltensperger, U., Rudich, Y., Simpson, D., Claeys, M., Dommen, J., Donahue, N. M., George, C., Goldstein, A. H., Hamilton, J. F., Herrmann, H., Hoffmann, T., Iinuma, Y., Jang, M., Jenkin, M. E., Jimenez, J. L., Kiendler-Scharr, A., Maenhaut, W., McFiggans, G., Mentel, T. F., Monod, A., Prevot, A. S. H., Seinfeld, J. H., Surratt, J. D., Szmigielski, R., and Wildt, J.: The formation, properties and impact of secondary organic aerosol: Current and emerging issues, Atmos. Chem. Phys., 9, 5155-5236, 10.5194/acp-9-5155-2009, 2009.

Hinks, M. L., Montoya-Aguilera, J., Ellison, L., Lin, P., Laskin, A., Laskin, J., Shiraiwa, M., Dabdub, D., and Nizkorodov, S. A.: Effect of relative humidity on the composition of secondary organic aerosol from the oxidation of toluene, Atmos. Chem. Phys., 18, 1643-1652, 10.5194/acp-18-1643-2018, 2018.

Howard, C. J., and Evenson, K. M.: Kinetics of reaction of HO_2 with NO, Geophys. Res. Lett, 4, 437-440, 10.1029/GL004i010p00437, 1977.

Jang, M. S., Czoschke, N. M., Lee, S., and Kamens, R. M.: Heterogeneous atmospheric aerosol production by acid-catalyzed particle-phase reactions, Science, 298, 814-817, 10.1126/science.1075798, 2002.

Jaoui, M., Corse, E., Kleindienst, T. E., Offenberg, J. H., Lewandowski, M., and Edney, E. O.: Analysis of secondary organic aerosol compounds from the photooxidation of d-limonene in the presence of NOx and their detection in ambient PM2.5, Environ. Sci. Technol., 40, 3819-3828, 10.1021/es052566z, 2006.

Jia, L., and Xu, Y.: Effects of relative humidity on ozone and secondary organic aerosol formation from the photooxidation of benzene and ethylbenzene, Aerosol Sci. Tech., 48, 1-12, 10.1080/02786826.2013.847269, 2014.

Jia, L., and Xu, Y.: Ozone and secondary organic aerosol formation from Ethylene-NO (x)-NaCl irradiations under different relative humidity conditions, J. Atmos. Chem., 73, 81-100, 10.1007/s10874-015-9317-1, 2016.

Jia, L., and Xu, Y.: Different roles of water in secondary organic aerosol formation from toluene and isoprene, Atmos. Chem. Phys. Discuss., in review, org/10.5194/acp-2017-1064, 2017.

Jonsson, A. M., Hallquist, M., and Ljungstrom, E.: Impact of humidity on the ozone initiated oxidation of limonene, delta(3)-carene, and alpha-pinene, Environ. Sci. Technol., 40, 188-194, 10.1021/es051163w, 2006.

Kamens, R. M., Zhang, H., Chen, E. H., Zhou, Y., Parikh, H. M., Wilson, R. L., Galloway, K. E., and Rosen, E. P.: Secondary organic aerosol formation from toluene in an atmospheric hydrocarbon mixture: Water and particle seed effects, Atmos. Environ., 45, 2324-2334, 10.1016/j.atmosenv.2010.11.007, 2011.

Kanakidou, M., Seinfeld, J. H., Pandis, S. N., Barnes, I., Dentener, F. J., Facchini, M. C., Van Dingenen, R., Ervens, B., Nenes, A., Nielsen, C. J., Swietlicki, E., Putaud, J. P., Balkanski, Y., Fuzzi, S., Horth, J., Moortgat, G. K., Winterhalter, R., Myhre, C. E. L., Tsigaridis, K., Vignati, E., Stephanou, E. G., and Wilson, J.: Organic aerosol and global climate modelling: A review, Atmos. Chem. Phys., 5, 1053-1123, 10.5194/acp-5-1053-2005, 2005.

Koch, B. P., Witt, M. R., Engbrodt, R., Dittmar, T., and Kattner, G.: Molecular formulae of marine and terrigenous dissolved organic matter detected by electrospray ionization Fourier transform ion cyclotron resonance mass spectrometry, Geochim. Cosmochim. Ac., 69, 3299-3308, 10.1016/j.gca.2005.02.027, 2005.

Kroll, J. H., Ng, N. L., Murphy, S. M., Flagan, R. C., and Seinfeld, J. H.: Secondary organic aerosol formation from isoprene photooxidation, Environ. Sci. Technol., 40, 1869-1877, 10.1021/es0524301, 2006.

Kroll, J. H., and Seinfeld, J. H.: Chemistry of secondary organic aerosol: Formation and evolution of low-volatility organics in the atmosphere, Atmos. Environ., 42, 3593-3624, 10.1016/j.atmosenv.2008.01.003, 2008.

Kulmala, M., Kontkanen, J., Junninen, H., Lehtipalo, K., Manninen, H. E., Nieminen, T., Petaja, T., Sipila, M., Schobesberger, S., Rantala, P., Franchin, A., Jokinen, T., Jarvinen, E., Aijala, M., Kangasluoma, J., Hakala, J., Aalto, P. P., Paasonen, P., Mikkila, J., Vanhanen, J., Aalto, J., Hakola, H., Makkonen, U., Ruuskanen, T., Mauldin, R. L., III, Duplissy, J., Vehkamaki, H., Back, J., Kortelainen, A., Riipinen, I., Kurten, T., Johnston, M. V., Smith, J. N., Ehn, M., Mentel, T. F., Lehtinen, K. E. J., Laaksonen, A., Kerminen, V.-M., and Worsnop, D. R.: Direct observations of atmospheric aerosol nucleation, Science, 339, 943-946, 10.1126/science.1227385, 2013.

Liljegren, J. A., and Stevens, P. S.: Kinetics of the reaction of OH radicals with 3-methylfuran at low pressure, Int. J. Chem. Kinet., 45, 787-794, 10.1002/kin.20814, 2013.

Lim, Y. B., Tan, Y., Perri, M. J., Seitzinger, S. P., and Turpin, B. J.: Aqueous chemistry and its role in secondary organic aerosol (SOA) formation, Atmos. Chem. Phys., 10, 10521-10539, 10.5194/acp-10-10521-2010, 2010.

Lin, Y.-H., Zhang, Z., Docherty, K. S., Zhang, H., Budisulistiorini, S. H., Rubitschun, C. L., Shaw, S. L., Knipping, E. M., Edgerton, E. S., Kleindienst, T. E., Gold, A., and Surratt, J. D.: Isoprene epoxydiols as precursors to secondary organic aerosol formation: Acid-catalyzed reactive uptake studies with authentic compounds, Environ. Sci. Technol., 46, 250-258, 10.1021/es202554c, 2012.

Liu, S., Jia, L., Xu, Y., Tsona, N. T., Ge, S., and Du, L.: Photooxidation of cyclohexene in the presence of SO_2: SOA yield and chemical composition, Atmos. Chem. Phys., 17, 13329-13343, 10.5194/acp-17-13329-2017, 2017.

Mahowald, N., Ward, D. S., Kloster, S., Flanner, M. G., Heald, C. L., Heavens, N. G., Hess, P. G., Lamarque, J.-F., and Chuang, P. Y.: Aerosol impacts on climate and biogeochemistry, in, Annu. Rev. Env. Resour., 45-74, 2011.

Malm, W. C., Sisler, J. F., Huffman, D., Eldred, R. A., and Cahill, T. A.: Spatial and seasonal trends in particle concentration and optical extinction in the United States J. Geophys. Res., 99, 1347-1370, 10.1029/93jd02916, 1994.

Ng, N. L., Chhabra, P. S., Chan, A. W. H., Surratt, J. D., Kroll, J. H., Kwan, A. J., McCabe, D. C., Wennberg, P. O., Sorooshian, A., Murphy, S. M., Dalleska, N. F., Flagan, R. C., and Seinfeld, J. H.: Effect of NOx level on secondary organic aerosol (SOA) formation from the photooxidation of terpenes, Atmos. Chem. Phys., 7, 5159-5174, 10.5194/acp-7-5159-2007, 2007.

Odum, J. R., Jungkamp, T. P. W., Griffin, R. J., Flagan, R. C., and Seinfeld, J. H.: The atmospheric aerosol-forming potential of whole gasoline vapor, Science, 276, 96-99, 10.1126/science.276.5309.96, 1997.

Penkett, S. A.: Chemistry of the natural atmosphere, Nature, 336, 322-322, 10.1038/336322a0, 1988.

Pope, C. A., III, Ezzati, M., and Dockery, D. W.: Fine particulate air pollution and life expectancies in the United States: The role of influential observations, J. Air Waste Manage., 63, 129-132, 10.1080/10962247.2013.760353, 2013.

Ravishankara, A. R.: Are chlorine atoms significant tropospheric free radicals?, P. Natl. Acad Sci. USA, 106, 13639-13640, 10.1073/pnas.0907089106, 2009.

Riva, M., Barbosa, T. D. S., Lin, Y.-H., Stone, E. A., Gold, A., and Surratt, J. D.: Chemical characterization of organosulfates in secondary organic aerosol derived from the photooxidation of alkanes, Atmos. Chem. Phys., 16, 11001-11018, 10.5194/acp-16-11001-2016, 2016.

Russell, L. M., Bahadur, R., and Ziemann, P. J.: Identifying organic aerosol sources by comparing functional group composition in chamber and atmospheric particles, P. Natl. Acad Sci. USA, 108, 3516-3521, 10.1073/pnas.1006461108, 2011.

Sakamoto, Y., Inomata, S., and Hirokawa, J.: Oligomerization reaction of the criegee intermediate leads to secondary organic aerosol formation in ethylene ozonolysis, J. Phys. Chem. A, 117, 12912-12921, 10.1021/jp408672m, 2013.

Sareen, N., Waxman, E. M., Turpin, B. J., Volkamer, R., and Carlton, A. G.: Potential of aerosol liquid water to facilitate organic aerosol formation: Assessing knowledge gaps about precursors and partitioning, Environ. Sci. Technol., 51, 3327-3335, 10.1021/acs.est.6b04540, 2017.

Song, C., Na, K. S., and Cocker, D. R.: Impact of the hydrocarbon to NOx ratio on secondary organic aerosol formation, Environ. Sci. Technol., 39, 3143-3149, 10.1021/es0493244, 2005.

Song, C., Zaveri, R. A., Alexander, M. L., Thornton, J. A., Madronich, S., Ortega, J. V., Zelenyuk, A., Yu, X.-Y., Laskin, A., and Maughan, D. A.: Effect of hydrophobic primary organic aerosols on secondary organic aerosol formation from ozonolysis of alpha-pinene, Geophys. Res. Lett, 34, 10.1029/2007gl030720, 2007.

Spittler, M., Barnes, I., Bejan, I., Brockmann, K. J., Benter, T., and Wirtz, K.: Reactions of NO_3 radicals with limonene and alpha-pinene: Product and SOA formation, Atmos. Environ., 40, S116-S127, 10.1016/j.atmosenv.2005.09.093, 2006.

Tapia, A., Villanueva, F., Salgado, M. S., Cabanas, B., Martinez, E., and Martin, P.: Atmospheric degradation of 3-methylfuran: Kinetic and products study, Atmos. Chem. Phys., 11, 3227-3241, 10.5194/acp-11-3227-2011, 2011.

Varutbangkul, V., Brechtel, F. J., Bahreini, R., Ng, N. L., Keywood, M. D., Kroll, J. H., Flagan, R. C., Seinfeld, J. H., Lee, A., and Goldstein, A. H.: Hygroscopicity of secondary organic aerosols formed by oxidation of cycloalkenes, monoterpenes, sesquiterpenes, and related compounds, Atmos. Chem. Phys., 6, 2367-2388, 10.5194/acp-6-2367-2006, 2006.

Walser, M. L., Desyaterik, Y., Laskin, J., Laskin, A., and Nizkorodov, S. A.: High-resolution mass spectrometric analysis of secondary organic aerosol produced by ozonation of limonene, Phys. Chem. Chem. Phys., 10, 1009-1022, 10.1039/b712620d, 2008.

Wang, Y., Luo, H., Jia, L., and Ge, S.: Effect of particle water on ozone and secondary organic aerosol formation from benzene-NO_2-NaCl irradiations, Atmos. Environ., 140, 386-394, 10.1016/j.atmosenv.2016.06.022, 2016.

Xu, J., Griffin, R. J., Liu, Y., Nakao, S., and Cocker, D. R., III: Simulated impact of NOx on SOA formation from oxidation of toluene and m-xylene, Atmos. Environ., 101, 217-225, 10.1016/j.atmosenv.2014.11.008, 2015.

Yin, H., Yuan, H., Ye, Z., Li, S., and Liang, J.: Temporal and spatial distribution of VOCs and their OFP in the atmosphere of Chengdu, Acta Sci. Circumstantiae, 35, 386-393, 2015.

Yu, K.-P., Lin, C.-C., Yang, S.-C., and Zhao, P.: Enhancement effect of relative humidity on the formation and regional respiratory deposition of secondary organic aerosol, J. Hazard. Mater., 191, 94-102, 10.1016/j.jhazmat.2011.04.042, 2011.

Zhang, H., Surratt, J. D., Lin, Y. H., Bapat, J., and Kamens, R. M.: Effect of relative humidity on SOA formation from isoprene/NO photooxidation: enhancement of 2-methylglyceric acid and its corresponding oligoesters under dry conditions, Atmos. Chem. Phys., 11, 6411-6424, 10.5194/acp-11-6411-2011, 2011a.

Zhang, H., Lin, Y.-H., Zhang, Z., Zhang, X., Shaw, S. L., Knipping, E. M., Weber, R. J., Gold, A., Kamens, R. M., and Surratt, J. D.: Secondary organic aerosol formation from methacrolein photooxidation: Roles of NOx level, relative humidity and aerosol acidity, Environ. Chem., 9, 247-262, 10.1071/en12004, 2012a.

Zhang, Q., Jimenez, J. L., Canagaratna, M. R., Ulbrich, I. M., Ng, N. L., Worsnop, D. R., and Sun, Y.: Understanding atmospheric organic aerosols via factor analysis of aerosol mass spectrometry: A review, Anal. Bioanal. Chem., 401, 3045-3067, 10.1007/s00216-011-5355-y, 2011b.

Zhang, Y., Wang, X., Blake, D. R., Li, L., Zhang, Z., Wang, S., Guo, H., Lee, F. S. C., Gao, B., Chan, L., Wu, D., and Rowland, F. S.: Aromatic hydrocarbons as ozone precursors before and after outbreak of the 2008 financial crisis in the Pearl River Delta region, south China, J. Geophys. Res., 117, 10.1029/2011jd017356, 2012b.

Zhou, Y., Zhang, H., Parikh, H. M., Chen, E. H., Rattanavaraha, W., Rosen, E. P., Wang, W., and Kamens, R. M.: Secondary organic aerosol formation from xylenes and mixtures of toluene and xylenes in an atmospheric urban hydrocarbon mixture: Water and particle seed effects (II), Atmos. Environ., 45, 3882-3890, 10.1016/j.atmosenv.2010.12.048, 2011.

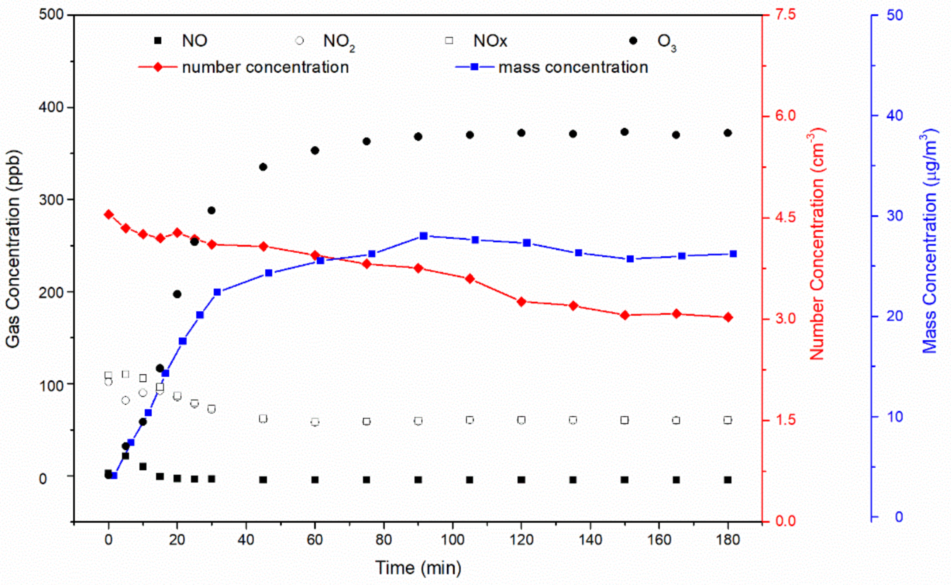

Figure 1: Profile of the gas-phase concentrations of reactants (NO, NO_2, NOx and O_3) and particle number/mass concentrations (wall loss corrected) over time. The C_4H_4O/NOx ratio is 7.91 and RH = 23 %. Since the particle wall loss has a weak RH dependence in our chamber, a mean value of 4.7×10^{-5} s^{-1} was used for wall loss correction. A density of 1.4 g cm^{-3} was used in the SMPS.

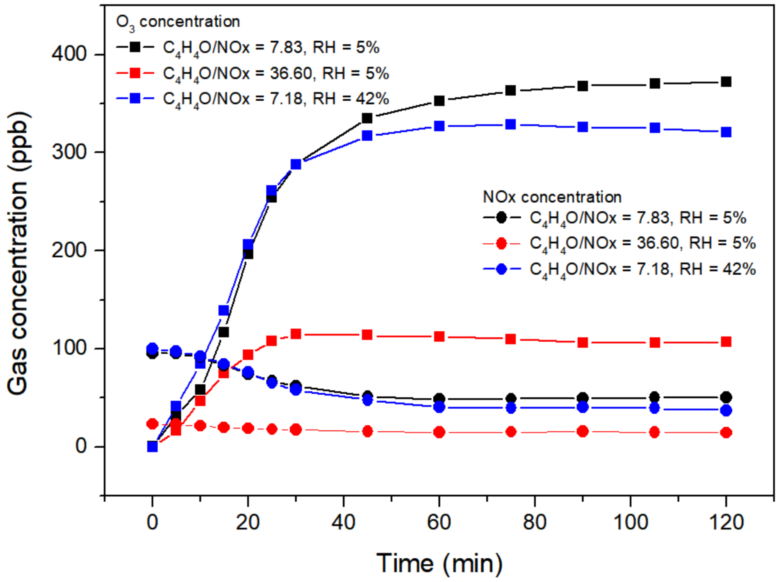

Figure 2: Comparisons of the observed concentrations of O_3 (square) and NOx (circle) from furan irradiations at different experimental conditions.

Atmos. Chem. Phys. Discuss., https://doi.org/10.5194/acp-2018-477
Manuscript under review for journal Atmos. Chem. Phys.
Discussion started: 25 June 2018

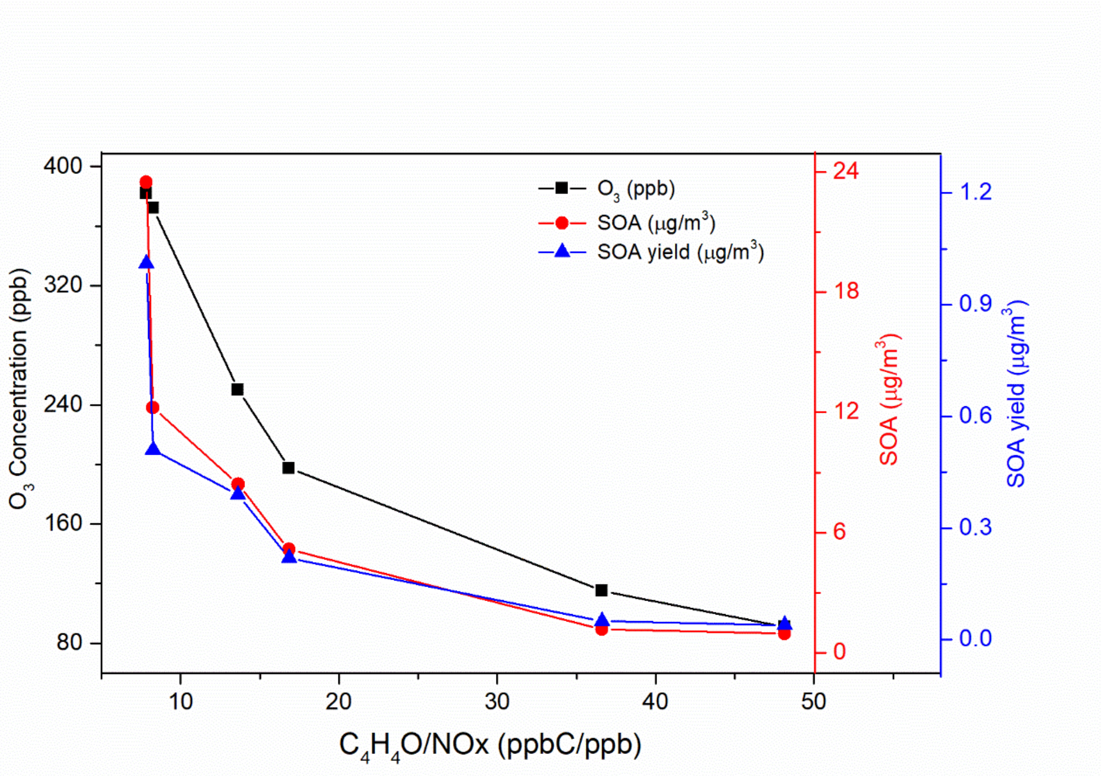

Figure 3: Dependences of the O_3 maximum concentration, SOA mass concentration and SOA yield on the C_4H_4O/NOx ratio. Since the particle wall loss has a weak RH dependence in our chamber, a mean value of 4.7×10^{-5} s^{-1} was used for wall loss correction. A density of 1.4 g cm^{-3} was used in SMPS.

5

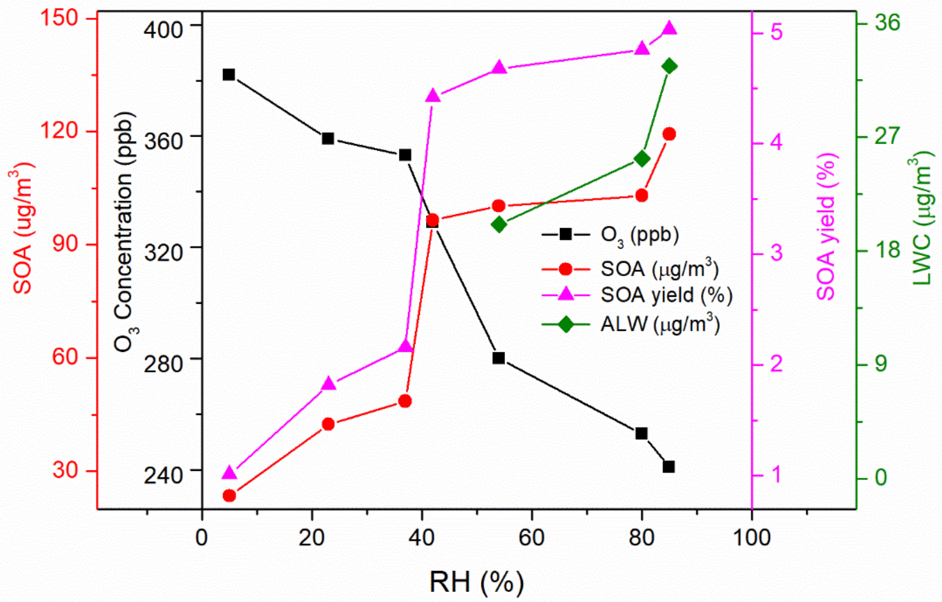

Figure 4: Dependences of O_3 maximum concentration, SOA mass concentration, SOA yield and ALW on relative humidity (RH).

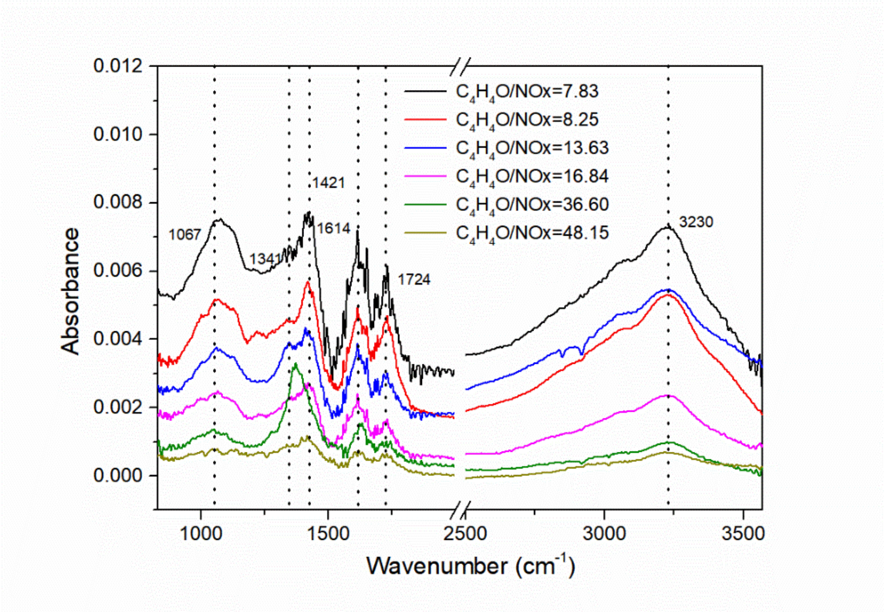

Figure 5: FTIR spectra of particles collected from furan-NOx-NaCl photooxidation experiments with different values of C_4H_4O/NOx ratio ranging from 7.83 to 48.15.

5

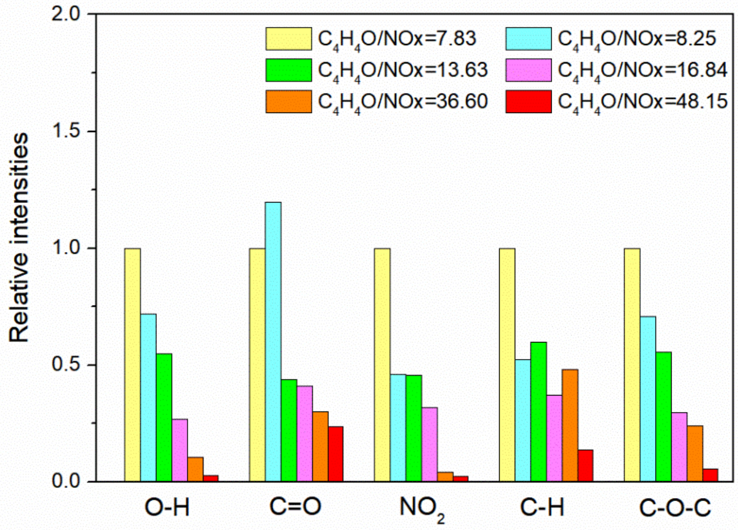

Figure 6: Variations of relative intensities of different functional groups with C_4H_4O/NOx ratios from 7.8 to 48.1.

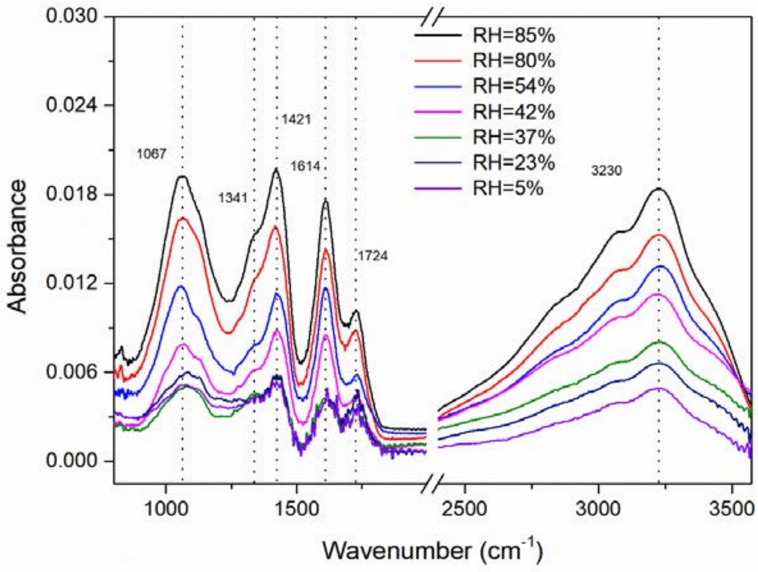

5 **Figure 7: FTIR spectra of particles collected from furan-NOx-NaCl photooxidation experiments with different values of RH ranging from 5 % to 85 %.**

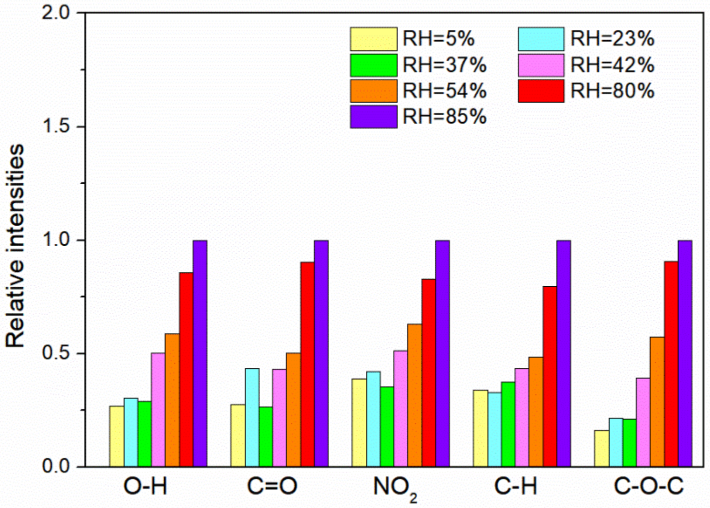

Figure 8: Variations of FTIR absorption intensities of different functional groups at RH from 5 % to 85 % relative to the intensity at 85 %.

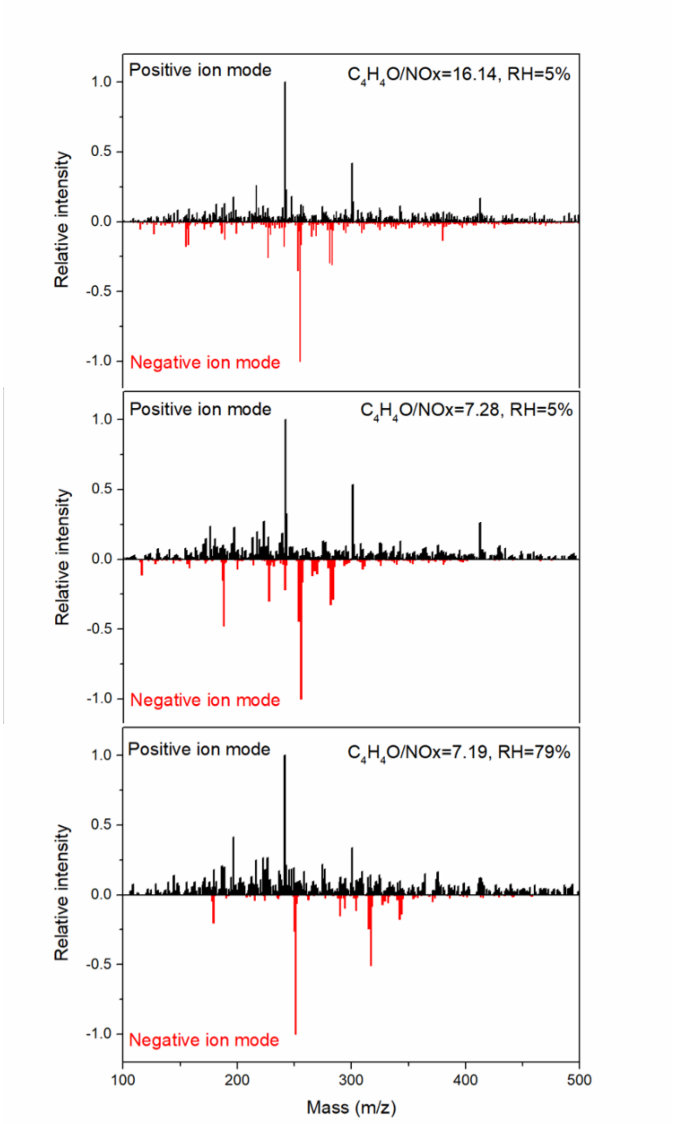

Figure 9: ESI-Exactive-Orbitrap MS spectra obtained in different experimental conditions. The black upward-pointing mass spectra represent the samples detected in positive ion mode and the red inverted mass spectra represent the samples detected in negative ion mode.

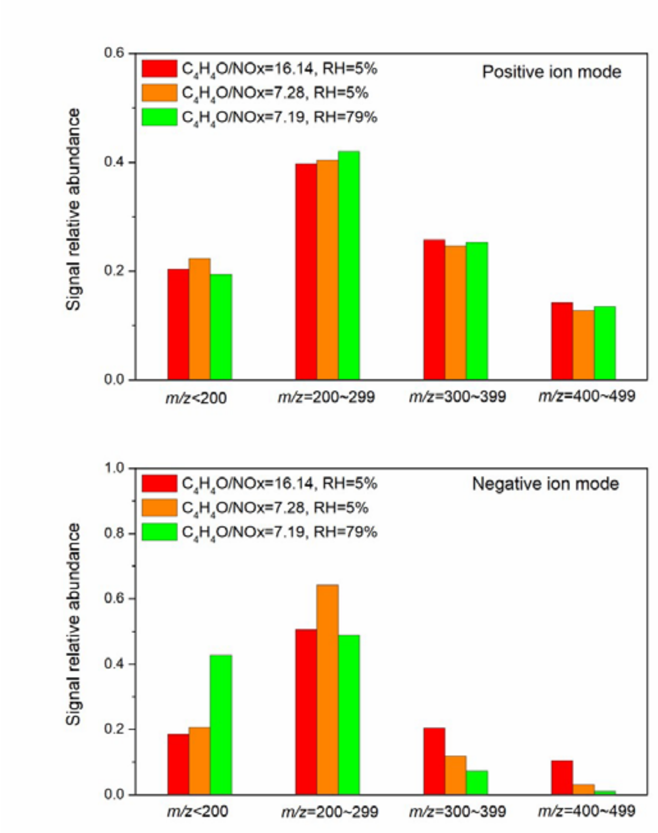

Figure 10: Signal relative abundance of ions detected by ESI-Exactive-Orbitrap MS in both positive and negative ion modes for all ranges of mass-to-charge ratios as identified in this work.

5

Table 1. Summary of initial conditions, O_3 concentrations and particle mass concentrations in furan-NOx-NaCl photooxidation experiments.

Exp No	Initial conditions						SOA formation results						
	$[\text{furan}]_0$ (ppb)	$[\text{NO}]_0$ (ppb)	$[\text{NO}_2]_0$ (ppb)	$[\text{NOx}]_0$ (ppb)	RH (%)	C_4H_4O/NOx (ppbC/ppb)	O_3 (ppb)	PM[a] (μg m^{-3})	NaCl[b] (μg m^{-3})	$NaNO_3$[c] (μg m^{-3})	ALW[d] (μg m^{-3})	SOA[e] (μg m^{-3})	SOA yield (%)
1	708.4	2.2	14.6	16.8	<5 %	48.15	91	12.2	11.22	3.53	--	0.96±0.10	0.04±0.01
2	749.0	2.0	21.2	23.2	<5 %	36.60	115	15.4	10.64	1.56	--	1.18±0.12	0.05±0.01
3	752.5	3.4	41.3	44.7	<5 %	16.84	197	21.3	14.06	2.08	--	5.15±0.51	0.22±0.02
4	705.8	5.5	46.3	51.8	<5 %	13.63	250	23.5	12.65	2.42	--	8.41±0.84	0.39±0.03
5	783.4	6.9	88.0	94.9	<5 %	8.25	372	29.1	13.46	3.38	--	12.23±1.22	0.51±0.05
6	763.4	6.1	91.4	97.5	<5 %	7.83	382	38.6	11.59	3.53	--	23.46±2.35	1.01±0.10
7	764.8	4.1	92.6	96.7	23 %	7.91	359	55.5	10.41	3.74	--	42.37±4.23	1.82±0.18
8	740.1	2.6	94.7	97.3	37 %	7.61	353	64.2	11.14	4.46	--	48.56±4.86	2.16±0.22
9	719.0	5.5	94.7	100.2	42 %	7.18	329	111.1	9.43	5.14	--	96.49±9.64	4.42±0.44
10	704.8	3.3	89.6	92.8	54 %	7.60	280	138.7	12.05	6.27	20.1	100.27±10.02	4.68±0.47
11	699.3	7.4	95.5	102.9	80 %	6.80	253	144.1	8.14	7.60	25.3	103.02±10.30	4.85±0.48
12	780.7	4.7	93.4	98.1	85 %	7.96	241	173.0	10.00	11.11	32.6	119.29±10.49	5.03±0.50
13	750.6	3.9	42.6	46.5	<5 %	16.14	for ESI-Exactive-Orbitrap MS analysis						
14	723.1	5.8	93.4	99.2	<5 %	7.28							
15	740.3	7.4	95.5	102.9	79 %	7.19							

[a]PM: particle mass concentration in the chamber was determined from the SMPS and was the sum of NaCl, $NaNO_3$, ALW and SOA at the end of the experiments.

[b]NaCl: the amount of NaCl at the end of the experiments;

[c]$NaNO_3$: the amount of $NaNO_3$ at the end of the experiments;

[d]ALW: the amount of aerosol liquid water content at the end of the experiments;

[e]SOA: the amount of secondary organic aerosol at the end of the experiments.

Table 2. Assignment of the observed FTIR absorption frequencies (cm^{-1}).

5

Absorption frequencies	Functional group	Assignment
1222-868	C-C and C−O	Stretching in alcohols (Coury and Dillner, 2008) C−O of COOH group (Duarte et al., 2005)
1067	C−O−C	C−O−C stretching (Jang et al., 2002)
1515-1350	CH_2, CH_3,	Bending vibration of CH_2 and CH_3 groups
1614, 1341	RNO_2	Polar nitro groups (Bruns et al., 2010)
1724	C=O	Stretching vibration in carboxylic acid and ketones
3000-2850	C−H	C−H stretching vibration in saturated carbon ring
3100-3000	C−H	C−H stretching vibration in unsaturated alkene
3200-2400	O−H	Stretching vibration in carboxyl groups
3100-3500	O−H	Stretching vibration in hydroxyl groups

Table 3. Ion peaks with the five most abundant compounds observed in ESI-Exactive-Orbitrap MS. Proposed assignments are based on the formulas from ESI-Exactive-Orbitrap MS. Peak abundances are normalized with respect to the most abundant peak in each spectrum.

No	Nominal mass (m/z)	Formula	C_4H_4O/NOx=16.14 RH=5 %	C_4H_4O/NOx=7.28 RH=5 %	C_4H_4O/NOx=7.19 RH=79 %
	Positive ion mode		Normalized peak abundance		
1	194	$C_{11}H_{16}O_2N$	0.02	0.01	0.02
2	242	$C_{14}H_{28}O_2N$	1.00	1.00	1.00
3	301	$C_{13}H_{21}O_6N_2$	0.41	0.53	0.34
4	333	$C_{13}H_{21}O_8N_3$	0.03	0.04	0.05
5	413	$C_{21}H_{37}O_6N_2$	0.16	0.26	0.12
	Negative ion mode		Normalized peak abundance		
6	157	$C_8H_{15}O_2N$	0.16	0.06	0.04
7	187	$C_9H_{17}O_3N$	0.07	0.48	1.00
8	227	$C_{11}H_{17}O_4N$	0.26	0.3	0.15
9	255	$C_{17}H_{31}O_2N$	1.00	1.00	0.51
10	281	$C_{18}H_{33}O_2$	0.30	0.33	0.18